

# A Photonic Tautochrone

W. Verstraelen,<sup>1,2,\*</sup> S. Zanotti,<sup>1,\*</sup> N. W. E. Seet,<sup>1,2</sup> J. Zhao,<sup>1</sup> D. Sanvitto,<sup>1,3</sup>  
J. Zuñiga-Perez,<sup>1,2</sup> K. Dini,<sup>1,†</sup> Y. G. Rubo,<sup>1,4,‡</sup> and T. C. H. Liew<sup>1,2,5,§</sup>

<sup>1</sup>*Division of Physics and Applied Physics, School of Physical and Mathematical Sciences,  
Nanyang Technological University 637371, Singapore*

<sup>2</sup>*Majulab International Joint Research Unit UMI 3654,  
CNRS, Université Côte d'Azur, Sorbonne Université,  
National University of Singapore, Nanyang Technological University, Singapore*

<sup>3</sup>*CNR NANOTEC Institute of Nanotechnology, Via Monteroni, Lecce 73100, Italy*

<sup>4</sup>*Instituto de Energías Renovables, Universidad Nacional Autónoma de México, Temixco, Morelos, Mexico*

<sup>5</sup>*Centre for Quantum Technologies, Nanyang Technological University Singapore*

(Dated: March 6, 2026)

We propose to implement an optical analogue of the tautochrone property of the cycloid to allow the focusing of ultrashort pulses inside photonic systems. This allows to enhance nonlinear effects, resulting in orders of magnitude increase of nonlinearity-induced phase shifts, while employing low irradiances. Building upon the optical-mechanical analogy, we show how to produce optical limiters for temporal light pulses, and how to implement temporal bistability and even multistability with large numbers of states. Finally, we move this concept to the quantum realm and predict a tautochrone quantum blockade regime with a stronger antibunching.

*Introduction.*— In classical mechanics, there exists a trajectory for which particles starting simultaneously to slide down under constant acceleration and with no friction can arrive at the end of the curve at exactly the same time even if they had started at different positions along the curve. This remarkable effect is known as the tautochrone property of the cycloid and has been exploited in the design of accurate pendulum clocks [1]. Here, we ask whether it is possible to implement an analogous tautochrone effect in a photonic system and what this implies in the presence of nonlinearity.

We must first address a slight difference between mechanics and optics: in mechanics, particles follow a cycloid curve in a uniform gravitational field, while in optics photons move in straight lines. Nevertheless, we can easily imagine media in which photons move in a spatially non-uniform potential, which can be constructed thanks to a spatially-varying refractive index or to an adapted geometry of the photonic medium in which they are propagating. The key to the existence of a tautochrone effect is a spatially-varying potential energy, not necessarily a curved path.

The nonlinear Schrödinger equation provides a description of light propagating in nonlinear media. For photonic particles with a parabolic dispersion and parabolic potential in the direction transverse to propagation, it can be written as:

$$i\frac{\partial\psi(\mathbf{x},t)}{\partial t} = \frac{1}{2}(-\nabla^2 + \mathbf{x}^2 - i\gamma + 2|\psi(\mathbf{x},t)|^2)\psi(\mathbf{x},t) + F(\mathbf{x},t). \quad (1)$$

This equation describes, for example, the behaviour of light in planar Fabry-Perot microcavities, where light is confined in the microcavity growth direction but spreads in the plane  $\mathbf{x} = (x, y) = (r \cos \phi, r \sin \phi)$ . In such a case,

dissipation is accounted for with rate  $\gamma$ , the nonlinear term represents a Kerr-type nonlinearity, and  $F$  represents the amplitude of a coherent driving field (e.g., a laser source). We use dimensionless units (see the Appendix for transformation to real variables).

If the system is driven with an ultrashort laser pulse that is also spatially wide, light is injected at different positions in space at the same moment of time. If the pulse is only slowly varying in the transverse coordinate, which is commonly the case for a laser pulse aligned with the propagation direction (or growth direction for microcavities), we can note that the initial energy of the light is dominated by its potential energy, while its kinetic energy is initially vanishing. This is analogous to the initial conditions of classical particles initialized on a cycloid curve with zero velocity.

Given that the oscillation frequency of particles in a parabolic potential is independent of their energy, every particle is now accelerated toward the center of the parabolic potential and will reach  $\mathbf{x} = 0$  at the same time (see Fig. 1a). In the linear regime without dissipation, an initial Gaussian wavepacket evolves as  $|\psi(t, \mathbf{x})|^2 \propto \exp\{-\mathbf{x}^2/(2|\sigma(t)|^2)\}$  (see, e.g., Ref. [2] and Supplemental Material for full solution), where the time evolution of the width is:

$$|\sigma(t)|^2 = \sigma_0^2 \cos^2 t + \frac{1}{4\sigma_0^2} \sin^2 t, \quad (2)$$

and  $\sigma_0 = \sigma(0)$  defines the initial width. We note that for a large enough initial width, the wavepacket collapses to a point. This behaviour is shown in Fig. 1b. While in theory larger and larger initial widths give arbitrarily tighter focusing, we should note that the paraxial approximation will eventually break down in this simple picture. In any case, a strong focusing effect is clearly achieved.

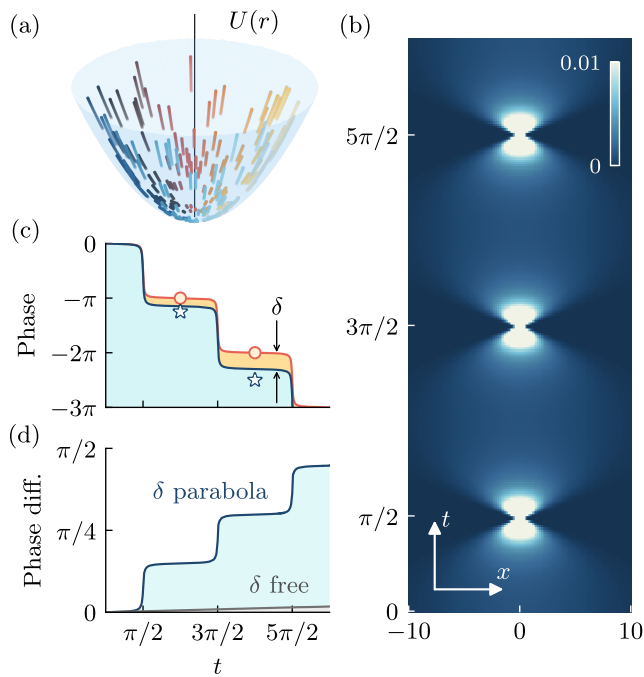


FIG. 1. **Photonic Tautochrone.** a) A pulsed excitation initializes particles at different positions of a parabolic potential. The particles are then accelerated toward the center corresponding to a focusing of light. b) A space-time plot of intensity at  $y = 0$  shows that the focusing occurs at  $t = \pi/2$  and integer delays of  $\pi$  thereafter. The colour scale has been saturated at  $1/100$  the peak value. c) The phase of light in the center undergoes a jump of  $\pi$  after each focusing event (red); the shift is enhanced in the nonlinear regime (blue). Circles and stars mark the times and phases of the excitation pulses for the optical limiter and bistable regimes, respectively. d) Nonlinearity-induced phase shift for free particles (grey) and in the presence of a parabolic potential (blue). The initial field  $\psi(x)$  is normalized to unity. Other parameters:  $\sigma_0 = 5$ ;  $\gamma = 0$ .

We propose that the aforementioned focusing effect can have strong implications in nonlinear photonics by enhancing the effect of interactions in nonlinear media. We show theoretically that it allows orders of magnitude enhancement of nonlinear phase shifts, temporal bistability, temporal multistability, and quantum blockade. Most importantly from the experimental point of view, we also present explicit designs of photonic structures for the realization of the required photonic potential.

*Interaction-induced phase-shift.*— While the simplest way to detect interactions in a nonlinear photonic system is to look for an energy shift of the photonic modes involved, the most accurate measurements, which have sensitivity down to the few photon level [4], rely on phase shifts. In Fig. 1c, we find that the phase shift measured in the center of a two-dimensional parabolic potential jumps by  $\pi$  in the linear regime every time the particles undergo a focusing event. The phase shift is enhanced in

the nonlinear regime and we define the nonlinear-induced phase shift as the difference of the phase in the nonlinear and linear regimes in Fig. 1d. Remarkably, the nonlinear-induced phase shift is over two orders of magnitude larger in the parabolic trap as compared to the same pulse without the parabolic potential and the same nonlinear interaction strength.

*Optical Limiter.*— Aside the prospect of enhanced nonlinear-induced phase shifts, we can also ask if related nonlinear intensity effects would also be enhanced. Among the most fundamental of Kerr nonlinear effects is the optical limiter effect, whereby the injected intensity from a resonant continuous wave laser increases sublinearly with the laser power and which is used to protect devices from overload (including lasers themselves). This effect relies on interactions shifting the photonic field out of resonance with the pumping laser. To achieve this in the tautochrone case we should ensure that all light is injected at the same time, which would necessitate using short pulses and, thus, restricting to broadband photonic fields and driving fields. Instead, we propose to consider a periodic driving of the system with a sequence of ultrashort pulses whose period matches twice the focusing time.

In the absence of interactions, we obtain the result shown in Fig. 2a. Here we have also ensured that subsequent pulses have a phase shift of  $\pi$  and are spatially inverted such that each pulse adds constructively to the field and respects  $F(\mathbf{x}, t = (2n + 1)\pi) = -F(-\mathbf{x}, t = 2n\pi)$ . We account now also for dissipation, considering the regime where the dissipation (lifetime) is comparable to the repetition period. In Fig. 2b, we find that in the nonlinear regime the intensity is significantly reduced. This is because the nonlinear phase shifts desynchronize the signal from the driving pulses.

Figure 3(a) shows that the increase of the photonic field intensity with laser power in the aforementioned pulsed excitation case follows an optical limiter-like curve. This curve appears more nonlinear for the same range of (time-averaged) field intensity when compared to the traditional optical limiter achieved under continuous wave excitation, as represented by the almost linear dependence shown in Figure 3(a) (for a fair comparison between the pulsed and CW regimes, we consider the same parabolic potential and dissipation rate).

*Bistability.*— Aside the optical limiter effect, a Kerr nonlinear resonator can also demonstrate bistability under continuous wave excitation [5] when the driving field is tuned slightly out of resonance. To make use of the tautochrone mechanism, we consider an extension of the phase delay between subsequent pulses exploited in the optical limiter effect as an analogue of the detuning in the continuous wave bistable regime. Notably, the excitation pulses remain on resonance, in contrast to conventional bistability schemes based on frequency detuning. Figure 3b shows that an extra  $0.25\pi$  dephasing of the pumps

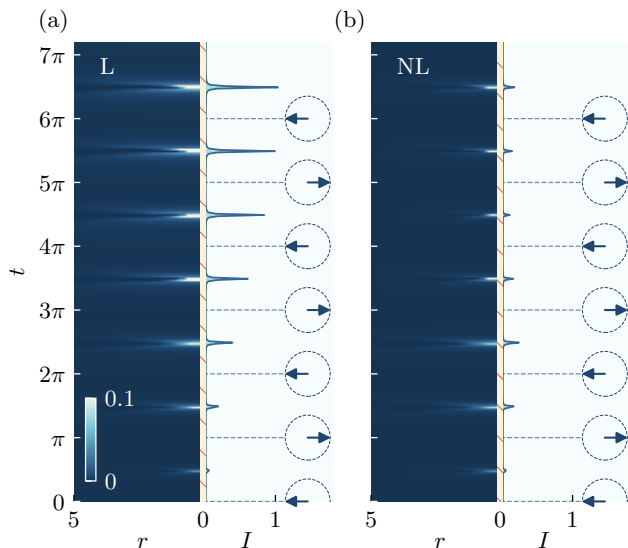


FIG. 2. **Pulsed Excitation.** (a) Intensity  $|\psi(r, t)|^2$  (left) and its linecut at  $r = 0$  (right) under periodic excitation without interactions, computed from Eq. 1 ( $\psi(r, \phi, t)$  is independent of  $\phi$ , so we do not plot the  $\phi$  dependence). The repetition period was  $\pi$ ,  $\gamma = 1/(2\pi)$ , and all other parameters were the same as in Fig. 1, with the spatially integrated pulse intensity set to unity. Arrows mark the pulse arrival times, and their orientation encodes the excitation phase; these pulses correspond to the circles shown in Fig. 1(c). We have chosen the driving term to have a Gaussian form in space. (b) Same analysis as in (a), but with nonlinear interaction included, which leads to a pronounced quenching of the peaks intensity. Intensities in (a) and (b) have been normalised to the maximum peak intensity in (a). For subsequent pulses, the system eventually settles in a state where the intensity is periodic in time.

compared to the optical limiter results in bistability and hysteresis in the system. The physical interpretation is that when there is a low intensity in the system, the focusing and defocusing sequence in the tautochrone is not synchronized with the phases of the repeating driving pulses. However, with some intensity in the system, interactions allow synchronization and maintenance of a high intensity. While traditionally bistability is used to describe a system with two stationary states of the system, we use the term here to describe two spatially and temporally oscillating states that are nevertheless stable and exist under the same conditions.

*Multistability.*—The aforementioned effect may seem like an over-complicated analogue of already well-established bistability. However, what is quite different to the usual bistability under continuous wave excitation is that the tautochrone mechanism allows generalization to support multiple stable states, with obvious potential applications in communication and information processing. We recall that the sequence of pulses excites an oscillating state that focuses and defocuses periodically. In addition to this state and its associated pulse

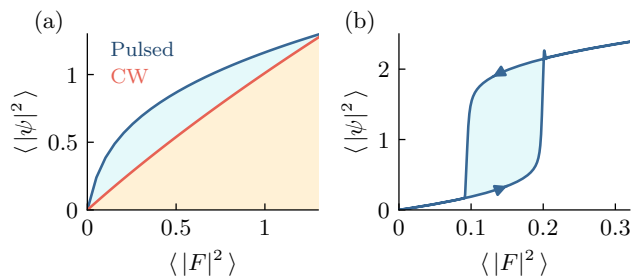


FIG. 3. **Optical Limiter & Bistability.** a) Power dependence of a photonic tautochrone under periodic pulsed excitation, compared to the same setup under continuous wave (CW) excitation.  $\langle |\psi|^2 \rangle$  and  $\langle |F|^2 \rangle$  represent spatially integrated and time-averaged field and driving intensities, respectively. Parameters were the same as in Fig. 2b. As the overall response to the CW excitation is weaker than the pulsed case,  $|F|^2$  is multiplied by a factor of 100 for CW excitation. b) Same as (a) but with the phase delay between subsequent pulses set to  $1.25\pi$ . The driving field intensity is slowly ramped up and down, revealing a hysteresis region (shaded).

sequence, we could apply another set of pulses at intermediate times. To minimise cross-interactions between the two pulse sequences, the pulse profile is chosen as a Gaussian multiplied by the square of the radial coordinate, so that the excitation vanishes at the centre. This would effectively enable to double the pulse repetition rate and allow for two states of light oscillating simultaneously in the system, with each state focusing with the arrival of alternate pulses. Figure 4 shows that four different spatially and temporally oscillating states are now supported under the same conditions.

Interestingly, the multistable regime can be easily generalized to generate a larger number of coexisting stable states. In the Appendix, instead of doubling the pulse repetition rate, we quadruple it and find that sixteen different stable states are supported under the same conditions.

*Quantum Blockade.*— So far, we have discussed a photonic tautochrone and its consequences in the nonlinear regime within the framework of semi-classical theory, including the optical limiter effect. This is appropriate for large numbers of particles where the mean-field approximation offers a good description of coherent states. Going beyond such an approximation, a quantum treatment of the conventional optical limiter (i.e., under continuous drive) gives rise to the photon [10] or polariton [11] blockade effect. While the classical optical limiter uses an optical density to shift out of resonance the optical field and the coherent driving field, the quantum blockade allows multiparticle quantum states to shift out of resonance and be effectively suppressed. The result is a non-classical antibunched state, characterized by a second order correlation function  $g^{(2)}$  dropping below 1 (for a multiparticle state) and approaching 0 for a perfect single particle state. For this effect to take place, one re-

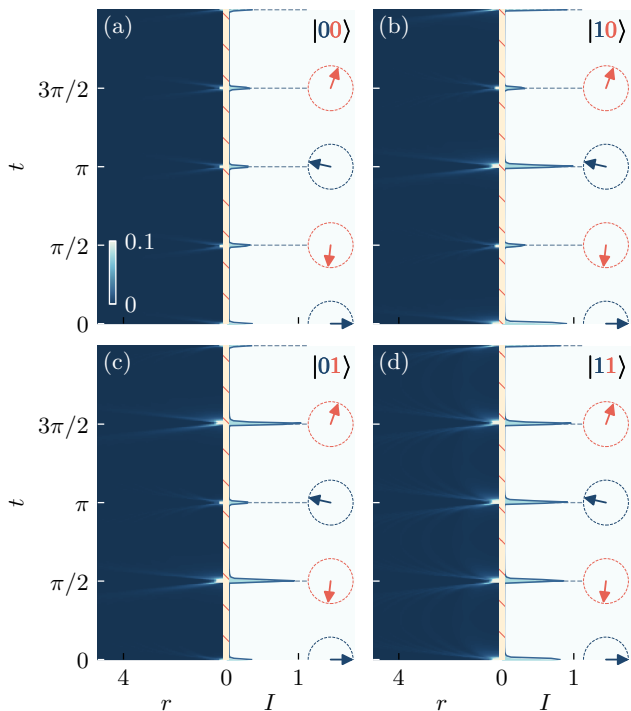


FIG. 4. **Multistability.** A photonic tautochrone is driven by two pulse trains with a repetition period of  $\pi/2$ , each encoding a different bit. Under these conditions, a hysteresis curve analogous to that in Fig. 3b is obtained, and the pulse intensity is chosen to operate within the multistable regime. Depending on the excitation history, four distinct oscillating states can be produced. Panels (a–d) correspond to the four possible bit encodings  $|00\rangle$ ,  $|01\rangle$ ,  $|10\rangle$ , and  $|11\rangle$ , respectively. All remaining parameters are the same as in Fig. 3b. The colour scales have been saturated to  $1/10$  of the peak intensity in (d). Unlike in Fig. 2, here we show the intensity after many pulses such that the initial transient dynamics has been completed.

quires the interaction strength between two particles to exceed the linewidth of the system.

While exciton-polaritons are known for their nonlinearity, which is stronger than in conventional nonlinear photonics, only the onset of the polariton blockade, with second order correlations below but still close to 1, have been attained experimentally [12, 13]. We note that such single photon states are, beyond fundamental interest, important building blocks for many applications, including quantum technologies such as quantum key distribution and boson sampling, as well as to biological research [29, 30].

We now consider a fully quantum theory of our photonic tautochrone, introducing the density matrix  $\rho$  to represent the quantum state of the system, which evolves according to the master equation:

$$i\hbar \frac{\partial \rho}{\partial t} = [\hat{\mathcal{H}}, \rho] + i\tilde{\gamma} \hat{\mathcal{L}}(\rho) \quad (3)$$

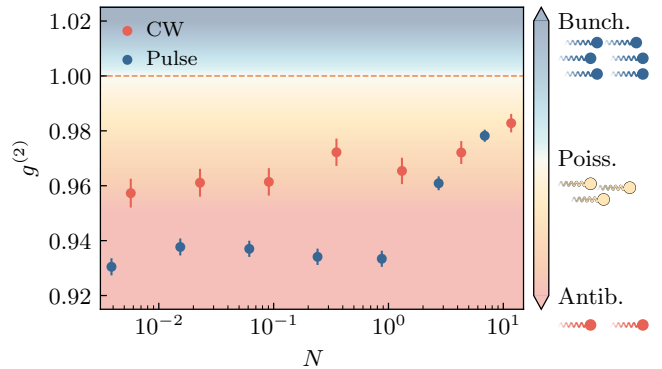


FIG. 5. **Photon blockade.** For sufficient photon nonlinearity  $\alpha$ , conventional photon blockade will shift the multi-photon states out of resonance causing antibunching, as is well known under continuous wave (CW) excitation, also in the parabolic trap. The enhancement of interactions through pulses in the tautochrone scheme however, is able to enhance such antibunching. Simulations were done over fixed  $\alpha = 0.1 \omega l^2$ , where  $l, \omega$  are the harmonic oscillator length and frequency, respectively, while varying  $F_0$ , which affects also the average particle number  $N$ . Refer to supplementary for details.

Here  $\hat{\mathcal{H}}$  is the Hamiltonian, which accounts for parabolic kinetic and potential energies together with nonlinear interactions and is defined in the Appendix. The Lindblad superoperator  $\hat{\mathcal{L}}$  describes the dissipation of particles at rate  $\tilde{\gamma}$ . Whereas the conventional quantum blockade is typically calculated for a single quantum mode, we do need to account for spatial dependence explicitly to model the tautochrone behaviour. While this approach results in an intractable size of the density matrix, the master equation can be simulated (to arbitrary accuracy) using a stochastic sampling of the phase space within the Positive P approach (see the Appendix for a full description). The full (equal time) second order correlation function of the trap created by the tautochrone effect is defined as:

$$g^{(2)}(t) = \frac{\iint \langle \hat{\psi}^\dagger(\mathbf{x}, t) \hat{\psi}^\dagger(\mathbf{x}', t) \hat{\psi}(\mathbf{x}', t) \hat{\psi}(\mathbf{x}, t) \rangle d^2\mathbf{x} d^2\mathbf{x}'}{\left( \int \langle \hat{\psi}^\dagger(\mathbf{x}, t) \hat{\psi}(\mathbf{x}, t) \rangle d^2\mathbf{x} \right)^2} \quad (4)$$

where  $\hat{\psi}(\mathbf{x}, t)$  annihilates a particle at position  $\mathbf{x}$  and time  $t$ ; the angled brackets denote the expectation value. Figure 5 compares the value of  $g^{(2)}$  under periodic pulsed excitation to that calculated under continuous wave excitation with the same spatial profile for the same parabolic potential. Although the mechanism of the optical limiter is somewhat different under periodic pulsed excitation, we find that it also results in antibunching in the quantum limit. More remarkably, the strength of the antibunching is twice as strong around  $N \sim 1$ . Modest system parameters were assumed, such that the conventional blockade under continuous wave excitation

matches experimental reports [12, 13]. Thus, even using realistic physical parameters, the tautochrone effect displays a clear quantitative advantage and appears as an interesting approach to enhance not only nonlinear effects but also, thanks to them, nonlinear quantum effects. In the next section we describe how to build a photonic system displaying the effect introduced in this work.

*Designs for Optical Potential Engineering.*— In principle, any photonic system with a spatially varying refractive index or effective refractive index would be suitable for the engineering of a parabolic potential for photons. Exciton-polaritons in microcavities are a good candidate system given that, indeed, parabolic traps have already been realized experimentally some time ago using different techniques to modify the local exciton-potential [6, 7] or the local photonic-potential thanks to a spatially varying cavity thickness [8]. In general, exciton-polaritons are renowned for their effective Kerr nonlinearity and there are, thus, also other options for potential engineering as described in [9]. Overall, the current fabrication state-of-the-art ensures the technological feasibility of microcavities implementing the necessary photonic or polaritonic potentials. For completeness, we give a complete theoretical simulation of such a system using nonlinear Maxwell-Bloch finite-difference time simulations in the Appendix (this also shows that our results are not dependent on the paraxial approximation implicit in Eq. 1).

*Discussion.*— One may wonder whether the aforementioned behavior could also occur with a non-parabolic potential or non-parabolic kinetic energy term. In a classical single-band model, the Hamiltonian for a particle in any one-dimensional potential can be written as a function of position  $x$  and momentum  $p$ . Regardless of the Hamiltonian, it could also be written in terms of the canonical variables  $I = (x^2 + p^2)/2$  and  $\theta = \text{atan}(x/p)$ . Here  $\theta = \pi/2$  corresponds to initial conditions where particles can have different values of position  $x$ , but zero momentum  $p$ ;  $\theta = \pi$  corresponds to the case where a particle has position  $x = 0$ . Hamilton’s equation of motion is  $\dot{\theta} = \partial H/\partial I$ . The only way for all particles to arrive at  $x = 0$  at the same time, regardless of their different initial positions (which give different values of  $I$ ), is to choose  $H \propto I$ , such that  $\dot{\theta}$  is independent of  $I$ . This implies a parabolic potential and parabolic kinetic energy. Mathematically, it appears that  $H$  could also be supplemented with some function of  $\theta$  without breaking the tautochrone behavior; however, such a dependence seems exotic from a physical point of view. Note that in a 2D case, similarly strong nonlinear effects could also be promoted by focusing particles on a line (caustic), and a wider class of effective Hamiltonians could lead to such behaviour.

We have focused on the excitation of a photonic tautochrone by a coherent pulsed excitation. One could also ask what happens under a non-resonant gain. Under a

simple Landau-Ginzburg type model [14], which is commonly used in the description of exciton-polariton lasers, we find that an effective optical limiter response can be realized above some threshold. This is quite different to the usual case of continuous wave excitation, where the Landau-Ginzburg model typically results in a linear growth of intensity above threshold. As the effects that we have discussed in this paper take the optical limiter effect as a foundation, we speculate that many of them would also be possible under non-resonant gain as well.

Finally, although we have considered a spatially uniform dissipation, systems with spatially varying dissipation could offer further advantages. A limitation of the conventional quantum blockade effect is that there is a large uncertainty in the time of generation of a single photon (which can be considered a consequence of the uncertainty principle and monochromatic frequency distribution). In principle, a system could be engineered so that dissipation is strongest at the center of the trap. This would allow a higher probability of emission at the specific times when the polychromatic wavepacket has focused to the trap center.

*Conclusion.*— An optical pulse in a medium with an effective parabolic potential becomes focused due to an analogue tautochrone property where all particles reach the center of the potential at the same time. This spatiotemporal focusing results in the enhancement of nonlinear-induced phase shifts by orders of magnitude. Despite the broad frequency range, analogues of the optical limiter effect, bistability, and multistability with large numbers of states can be arranged under periodic pulsed excitation. The periodic focusing of wavepackets results in an increased sensitivity to interactions, which ultimately manifests in a stronger quantum blockade.

*Acknowledgements.*— SZ, KD, JZP, & TCHL acknowledge support from the National Research Foundation grant N-GAP (NRF2023-ITC004-001). JZ & TCHL acknowledge support from the Singapore Ministry of Education (MOE) Academic Research Fund Tier 3 grant “Quantum Geometric Advantage” (MOE-MOET32023-0003). WV, DS, & TCHL acknowledge support from the EU under grant “Quantum Optical Networks based on Exciton-polaritons” (Q-ONE). NWES, JZP, DS, & TCHL acknowledge support from the EU under EIC Pathfinder Open project “Polariton Neuromorphic Accelerator” (PolArt, Id:101130304). YGR & TCHL acknowledge support from DGAPA-UNAM, Grant PAPIIT No. IN108524.

---

\* W. V. and S. Z. contributed equally to this work as first authors.

† kevin.dini74@gmail.com

‡ ygr@ier.unam.mx

§ timothyliew@ntu.edu.sg

- [1] R.A. Proctor, "A Treatise on the Cycloid and All Forms of Cycloidal Curves, and on the Use of Such Curves in Dealing with the Motions of Planets, Comets, &c., and of Matter Projected from the Sun", Longmans (1878).
- [2] D J Tannor, *Introduction to Quantum Mechanics: A Time-dependent Perspective* (Univ. Sci. Books, Sausalito, California, 2007).
- [3] I Carusotto & C Ciuti, *Rev. Mod. Phys.*, **85**, 299 (2013).
- [4] T Kuriakose, P M Walker, T Downing, O Kyriienko, I A Shelykh, P St-Jean, N Carlon Zambon, A Lemaitre, I Sagnes, L Legratier, A Harouri, S Ravets, M S Skolnick, A Amo, J Bloch, & D N Krizhanovskii, *Nature Photon.*, **16**, 566 (2022).
- [5] A Baas, J P Karr, H Eleuch, & E Giacobino, *Phys. Rev. A*, **69**, 023809 (2004).
- [6] R Balili, V Hartwell, D Snoko, L Pfeiffer, & K West, *Science*, **316**, 1007 (2007).
- [7] G Tosi, G Christmann, N G Berloff, P Tsotsis, T Gao, Z Hatzopoulos, P G Savvidis, & J J Baumberg, *Nature Phys.*, **8**, 190 (2012).
- [8] B Besga, C Vaneph, J Reichel, J Estève, A Reinhard, J Miguel-Sánchez, A Imamoğlu, & T Volz.
- [9] C Schneider, K Winkler, M D Fraser, M Kamp, Y Yamamoto, E A Ostrovskaya, & S Höfling, *Rep. Prog. Phys.*, **80**, 016503 (2017).
- [10] A Imamoğlu, R J Ram, S Pau, & Y Yamamoto, *Phys. Rev. A*, **53**, 4250 (1996).
- [11] A Verger, I Carusotto, & C Ciuti, *Phys. Rev. A*, **76**, 115324 (2007).
- [12] A Delteil, T Fink, A Schade, S Hofling, C Schneider, & A Imamoğlu, *Nature Mater.*, **18**, 219 (2019).
- [13] G Munoz-Matutano, A Wood, M Johnson, X Vidal Asensio, B Baragiola, A Reinhard, T Volz, A Lemaitre, J Bloch, A Amo, B Besga, & M Richard, *Nature Mater.*, **18**, 213 (2019).
- [14] J Keeling & N G Berloff *Phys. Rev. Lett.*, **100**, 250401 (2008).
- [15] M. Wei, W. Verstraelen, K. Orfanakis, Arvydas Ruseckas, Timothy C. H. Liew, Ifor D. W. Samuel, Graham A. Turnbull & Hamid Ohadi *Nat Commun* **13**, 7191 (2022).
- [16] K. Dini, H. Sigurdsson, N. W. E. Seet, P. M. Walker, and T. C. H. Liew *Phys. Rev. B* **110**, 214303 (2024).
- [17] N. W. E. Seet, K. Dini, S. Zanotti, J. Zúñiga-Pérez, T. C. H. Liew, *Nano Lett.*, **25**, 47, 16711–16716 (2025).
- [18] I Carusotto, C Ciuti, *Phys Rev B*.**72**,12 ,125335 (2005)
- [19] M Wouters, V Savona, *Phys. Rev. B* **79**, 16, 165302 (2009)
- [20] P. Deuar and A. Ferrier and M. Matuszewski and G. Orso and M. H. Szymańska, *PRX Quantum* **2** 1, 010319 (2021)
- [21] C. W. Gardiner, P. Zoller, *Quantum Noise: A handbook of markovian and non-Markovian Quantum stochastic methods with applications to Quantum Optics*, Springer, Berlin (2010)
- [22] A. Sinatra and C. Lobo and Y. Castin, *Journal of Physics B: Atomic, Molecular and Optical Physics*, **35** 17, 3599 (2002)
- [23] C Antón, T C H Liew, J Cuadra, M D Martín, P S Eldridge, Z Hatzopoulos, G Stavrinidis, P G Savvidis, and L. Viña, *Phys. Rev. B*, **88**, 035313 (2013).
- [24] I Carusotto, *Phys. Rev. A* **63**, 023610 (2001)
- [25] P D Drummond, D F Walls, *J Phys A: Math Gen* **13**, 725 (1980)
- [26] S Chaturvedi, C W Gardiner, I S Matheson, D F Walls, *J Stat Phys* **17**, 469 (1977)
- [27] N G Van Kampen, *Journal of Statistical Physics*, Vol. **24**, No. 1, (1981)
- [28] Milstein, Grigori N. ; Tretyakov, Michael V. *Stochastic numerics for Mathematical Physics*, Springer International Publishing AG (2022)
- [29] C. Couteau, S. Barz, T. Durt, T. Gerrits, J. Huwer, R. Prevedel, J. Rarity, A. Shields, and G. Weihs, "Applications of single photons to quantum communication and computing," *Nat. Rev. Phys.* **5**, 326–338 (2023).
- [30] C. Couteau, S. Barz, T. Durt, T. Gerrits, J. Huwer, R. Prevedel, J. Rarity, A. Shields, and G. Weihs, "Applications of single photons in quantum metrology, biology and the foundations of quantum physics," *Nat. Rev. Phys.* **5**, 354–363 (2023).
- [31] Discrete modes of size  $\Delta V_j$  are characterized by a set of annihilation operators  $\hat{a}_{x_j}$  and retrieve the canonical commutation relation  $[\hat{\psi}(\mathbf{x}), \hat{\psi}(\mathbf{x}')] = \delta^D(\mathbf{x}-\mathbf{x}')$  in  $D$  dimensions. We then define  $\hat{\psi}(x_j) = \lim_{\Delta V_j \rightarrow 0} \hat{a}_{x_j} / \sqrt{\Delta V_j}$ . The operator correspondences that allow mapping from  $\hat{\psi}, \hat{\psi}^\dagger$  to a pair of phase space variables  $\psi_p, \psi_p^\dagger$  are obtained straightforwardly from the discrete case [21] after which one proceeds as usual [24–26].

— SUPPLEMENTAL MATERIAL —

*Transformation of Eq. 1 to real units.*— We now introduce the conversion rules that connect the dimensionless formulation used in our calculations to the corresponding physical (dimensional) quantities.

We begin by defining the oscillator length  $l = \sqrt{\hbar/(m\omega)}$ , the natural spatial scale of a harmonic oscillator with frequency  $\omega$  and particle mass  $m$ . Although our calculations are performed in dimensionless units, the length  $l$  (together with the energy scale  $\hbar\omega$ ) provides the bridge back to physical units: all dimensional quantities can be reconstructed from these two characteristic scales.

In the following, dimensional variables are indicated by a tilde. The relations between dimensionless and dimensional variables are summarised by the conversion equations given below:

$$\tilde{\mathbf{x}} = l\mathbf{x}, \quad (\text{A1})$$

$$\tilde{t} = \frac{t}{\omega}, \quad (\text{A2})$$

$$\tilde{\psi} = \sqrt{\frac{\hbar\omega}{\alpha}} \psi e^{i\omega_p t}, \quad (\text{A3})$$

$$\tilde{\gamma} = \hbar\omega \gamma, \quad (\text{A4})$$

$$\tilde{F} = \sqrt{\frac{(\hbar\omega)^3}{\alpha}} F, \quad (\text{A5})$$

where:  $\alpha$  defines the strength of nonlinear interactions; and  $\omega_p$  represents the (central) angular frequency of laser excitation. In this case, Eq. 1 becomes:

$$i\hbar \frac{\partial \tilde{\psi}(\tilde{\mathbf{x}}, \tilde{t})}{\partial \tilde{t}} = \left( \hbar\omega_c - \frac{\hbar^2 \tilde{\nabla}^2}{2m} + \frac{1}{2} m\omega^2 \tilde{\mathbf{x}}^2 - \frac{i\tilde{\gamma}}{2} + \alpha |\tilde{\psi}(\tilde{\mathbf{x}}, \tilde{t})|^2 \right) \tilde{\psi}(\tilde{\mathbf{x}}, \tilde{t}) + \tilde{F}(\tilde{\mathbf{x}}, \tilde{t}) e^{-i\omega_p \tilde{t}}, \quad (\text{A6})$$

where  $\tilde{\nabla}^2$  is the Laplacian with respect to  $\tilde{\mathbf{x}}$  and  $\omega_c = \omega_p$ .

We note that all of our results are readily convertible to real units using Eqs. A1-A5, once the key parameters of the system are defined.

These conversions are also useful for estimating whether our scheme is feasible in a given photonic system. The dissipation rate is a critical parameter as it sets how much time is available for the focusing to occur. Equating the particle lifetime (given by  $\hbar/\tilde{\gamma}$ ) to the focusing time gives an estimate of the required angular frequency  $\omega_{\text{req}}$  of a given system:

$$\omega_{\text{req}} = \frac{\tilde{\gamma}\pi}{2\hbar} \quad (\text{A7})$$

Once  $\omega_{\text{req}}$  is defined, a typical limitation of a given physical system is that it would only be possible to engineer

the corresponding parabolic potential over a given energy range,  $E_{\text{max}}$ . This sets the maximum spatial range over which the potential can be engineered:

$$x_{\text{max}} = \sqrt{\frac{2E_{\text{max}}}{m\omega_{\text{req}}^2}} \quad (\text{A8})$$

One then attempts to excite the system with the largest spatial pulse width that fits within the range of the potential.

For example, a system with a lifetime of 50 ps and  $m = 3 \times 10^{-5} m_0$ , with  $m_0$  the free electron mass, would have a required potential strength  $m\omega_{\text{req}}^2 = 8.4 \times 10^{-3} \text{ meV } \mu\text{m}^{-2}$ . If it were possible to realize this potential over a range of  $E_{\text{max}} = 5 \text{ meV}$ , we would be able to work with  $x_{\text{max}} = 34 \mu\text{m}$ . This is enough to fit a pulse width of 21  $\mu\text{m}$ , which would correspond to the dimensionless  $\sigma_0 = 5$  considered in Fig. 1. A system with a longer lifetime, lighter effective mass, or larger range over which the potential can be realized would allow to operate with a larger value of  $\sigma_0$  and achieve a tighter focusing than that shown in Fig. 1.

Note that while we have defined rather than derived  $\omega_{\text{req}}$  in Eq. A7, it is based on an intuition. If we choose to operate with a smaller focusing frequency, then particles will have decayed before they can focus. If we choose to operate with a larger focusing frequency, then the spatial range over which particles can be focused (given that real physical systems have limits to the sizes of potentials that can be engineered) will be reduced according to Eq. A8.

*Analytic solution of Eq. (1) in linear regime.*— Neglecting nonlinear term and dissipation, Eq. (1) can be solved analytically for the case of an initial Gaussian wavepacket (equivalent to excitation with a delta function pulse in time with Gaussian profile in space). The solution is derived in a number of papers (see, e.g., [2]) and here we give the expressions in the form useful for qualitative understanding of possible effects of nonlinearities.

$$\begin{aligned} \psi(\mathbf{x}, t) &= \frac{1}{[2\pi\sigma^2(t)]^{d/4}} \exp\left\{-\frac{1}{2} \frac{\mu(t)}{\sigma(t)} \mathbf{x}^2\right\} \\ &= \frac{1}{[2\pi\sigma^2(t)]^{d/4}} \exp\left\{-[1 + i(\sigma_0^2 - \sigma_1^2) \sin(2t)] \frac{\mathbf{x}^2}{4|\sigma(t)|^2}\right\} \end{aligned} \quad (\text{A9})$$

where  $\sigma_0$  is the initial width of the pulse at  $t = 0$ ,  $\sigma_1 = 1/2\sigma_0$ ,  $\sigma(t) = \sigma_0 \cos(t) + i\sigma_1 \sin(t)$ ,  $\mu(t) = \sigma_1 \cos(t) + i\sigma_0 \sin(t)$ , and  $d$  is an integer representing the dimensionality of the system.

The phase  $\Phi$  of the wavepacket A9 at  $\mathbf{x} = 0$  is defined by the phase of the complex width  $\sigma(t)$ ,  $\Phi = -(d/2) \arctan[(\sigma_1/\sigma_0) \tan(t)]$ , and in the case of wide initial packet  $\sigma_0 \gg 1$  the phase exhibits sharp changes from 0 to  $-\pi d/2$ , then to  $-\pi d$ , etc. (see Fig. 1). The positions of these sharp drops correspond to collapse of the

wavepacket to the small width  $\sigma_1 \ll 1$  and the changes take place during the time  $\Delta t = 1/\sigma_0^2$  (FWHM of the peaks of  $-d\Phi/dt$ ). The nonlinearity becomes important for narrow wavepackets and it leads to an additional phase change, as shown in Fig. 1.

*Generalized Multistability.*— In Fig. 4 we showed that a doubling of the pulse repetition period allowed a generalization of bistability to multistability with four different spatially and temporally stable states under the same conditions. Fig. A1 shows the analogue of this figure, but instead with a quadrupling of the pulse repetition period. In this case, sixteen unique stable states can be identified.

We note that these results were attained choosing a pulse profile of the form:

$$F(\mathbf{x}) \propto \mathbf{x}^2 \exp(-\mathbf{x}^2/4\sigma_0^2) \quad (\text{A10})$$

Our system essentially operates as a linear system except at the specific moment and time when a given wavepacket focuses at the center of the trap. At this point, we want to minimize cross-interaction between wavepackets that are focusing and defocusing at different times. This is achieved by exciting with the above form that vanishes at the center.

*Schrödinger Equation with gain.*— Equation 1 of the main text considers a coherent driving field  $F(\mathbf{x}, t)$ . We can also consider the driving of the system by a non-resonant gain medium, modifying the Schrödinger equation to (this formalism is commonly used in the description of exciton-polariton condensates [14]):

$$i \frac{\partial \psi(\mathbf{x}, t)}{\partial t} = \frac{1}{2} (-\nabla^2 + \mathbf{x}^2 + iP(\mathbf{x}, t) - i\gamma + 2(1 - i\alpha_{\text{NL}})|\psi(\mathbf{x}, t)|^2) \psi(\mathbf{x}, t) \quad (\text{A11})$$

Here the gain  $P(\mathbf{x}, t)$  is assumed to be spatially and temporally controllable. As in the case of coherent driving, we consider driving with a Gaussian in space and periodic sequence of ultrashort pulses in time (taken as delta functions, for simplicity). The coefficient  $\alpha_{\text{NL}}$  represents the strength of nonlinear losses, which are needed to stabilize the gain process and maintain a finite intensity.

While in the main text, considering a two-dimensional system, we have found that the main effect of nonlinearity is to generate a phase shift, in a stronger nonlinear regime, we find that the focusing time can also be affected by interactions. For simplicity, we consider confinement into a one-dimensional system, taking  $\mathbf{x} = x$ . As shown in Fig. A2, we recover a sublinear growth of intensity with gain power, i.e., a similar optical limiter effect to the coherent driving case. The sublinear growth still requires overcoming of an initial threshold, but is otherwise strikingly different to the linear growth with intensity seen for the case of excitation with a continuous gain. The interpretation is that as the intensity increases, interactions delay the focusing so that it is desynchronized with the gain pulses.

*Quantum tautochrone model.*— The quantum dynamics of a setup such as discussed above is governed by the many-body Hamiltonian for driven interacting bosons which reads in the frame rotating at the driving frequency  $\omega_p$ :

$$\begin{aligned} \hat{\mathcal{H}} = & \int d^2\mathbf{x} \psi(\hat{\mathbf{x}})^\dagger \left( \frac{\mathbf{x}^2}{2} - \frac{\nabla^2}{2} - \Delta \right) \psi(\hat{\mathbf{x}}) \quad (\text{A12}) \\ & + \int d^2\mathbf{x} \int d^2\mathbf{x}' \frac{\alpha}{2} \delta(\mathbf{x} - \mathbf{x}') \hat{\psi}^\dagger(\mathbf{x}) \hat{\psi}^\dagger(\mathbf{x}') \hat{\psi}(\mathbf{x}') \hat{\psi}(\mathbf{x}) \\ & + \int d^2\mathbf{x} \left( F(\mathbf{x}, t) \hat{\psi}^\dagger(\mathbf{x}) + F^*(\mathbf{x}, t) \hat{\psi}(\mathbf{x}) \right). \end{aligned}$$

Note that we use the dimensionless units in terms of  $l, \omega, \hbar$  as discussed above. However, unlike the mean field case, the absolute particle number remains important, so that the contact interaction strength  $\alpha$  and coherent driving  $F$  must be explicitly considered. As in the classical case, we have  $F(\mathbf{x}) = F_0 \sqrt{\frac{\exp\{-\mathbf{x}^2/2\sigma_0^2\}}{2\pi\sigma_0^2}}$ .

Taking incoherent (constant) losses into consideration, the density matrix evolves as

$$\begin{aligned} \frac{d\hat{\rho}}{dt} = & -i[\hat{\mathcal{H}}, \hat{\rho}] \quad (\text{A13}) \\ & + \gamma \int d\mathbf{x} \left( \hat{\psi}(\mathbf{x}) \hat{\rho} \hat{\psi}^\dagger(\mathbf{x}) - \frac{\hat{\psi}^\dagger(\mathbf{x}) \hat{\psi}(\mathbf{x}) \hat{\rho} + \hat{\rho} \hat{\psi}^\dagger(\mathbf{x}) \hat{\psi}(\mathbf{x})}{2} \right) \end{aligned}$$

A numerical solution of A13 in a many-mode truncated Fock basis where  $\mathbf{x}$  is discretized (with lattice comparable with the mean-field simulations), would be intractably large. We therefore resort to phase space methods, which have shown advantage in such a case. In the context of polaritons, the truncated Wigner approximation (TWA) has been widely adopted historically [18, 19]. However, the TWA may suffer in modes with low occupation [22], which is the situation of interest here.

The Positive P method is an alternative, that is in principle exactly equivalent to (A13) [21]. Its convergence is not guaranteed, but is typically achieved in a strongly damped regime [20], and more appropriate for the purpose here. The formalism expands the density matrix of an  $N$ -mode system in the eigenbasis of  $N$ -mode coherent states  $\{\otimes_{j=1}^N |\beta_j\rangle\}$  and its conjugate  $\{\otimes_{j=1}^N \langle \beta_j^{+*} | \}$  ( $\beta^+$  generalises the role of  $\beta^*$  in the semiclassical Glauber-P distribution).

$$\hat{\rho} = \iint d\vec{\beta} d\vec{\beta}^+ \mathcal{P}(\beta_1, \dots, \beta_N; \beta_1^+, \dots, \beta_N^+) \bigotimes_{j=1}^N \frac{|\beta_j\rangle \langle \beta_j^{+*}|}{\langle \beta_j^{+*} | \beta_j \rangle}. \quad (\text{A14})$$

The master equation (A13) for  $\hat{\rho}$  is mapped on a Fokker-Planck equation for  $\mathcal{P}$ , which, in turn can be mapped on a set of stochastic differential equations using the

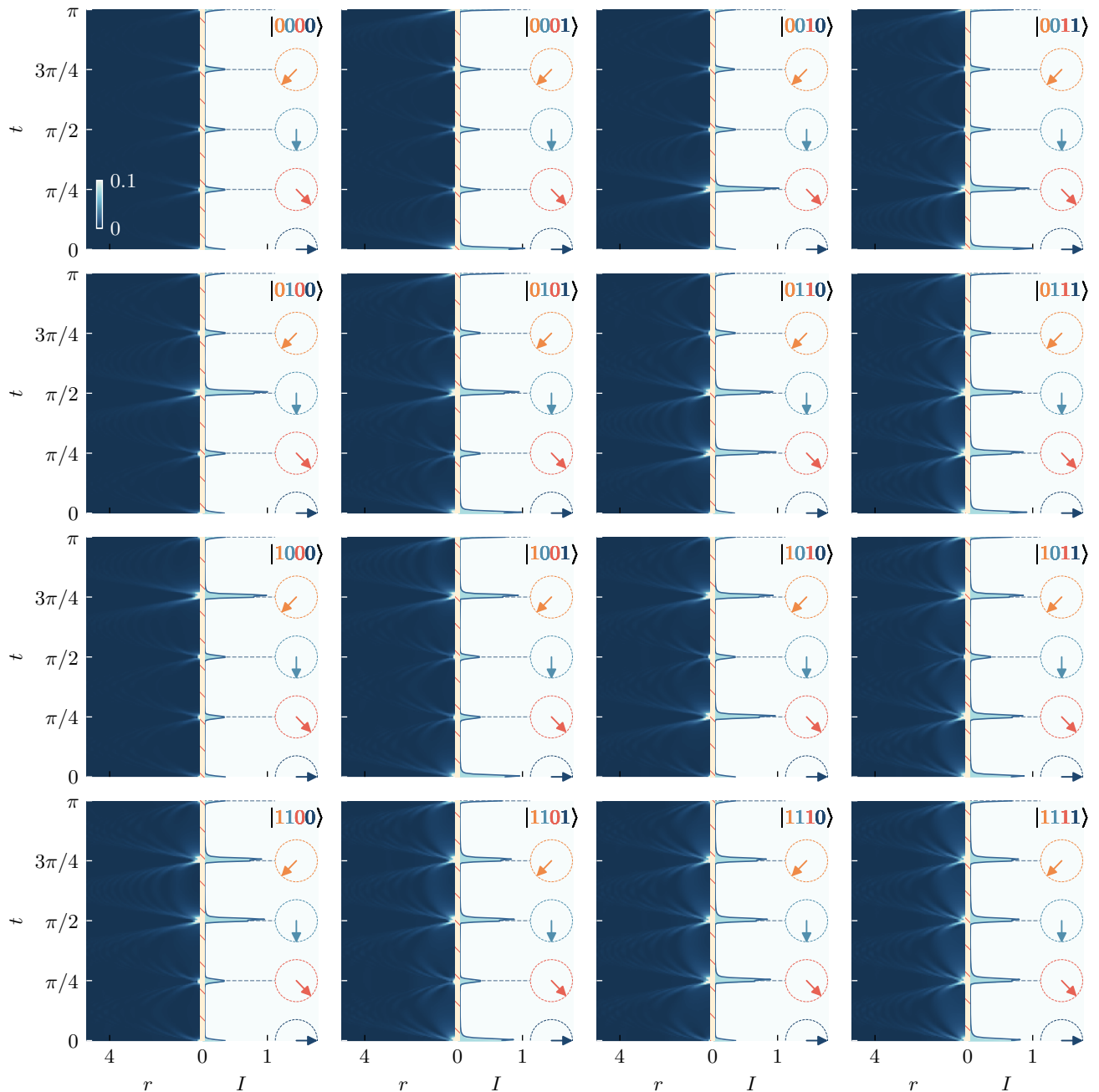


FIG. A1. **Multistability with sixteen states.** A photonic tautochrone is driven by four pulse trains with a repetition period of  $\pi/2$ , each encoding a different bit. Under these conditions, a hysteresis curve analogous to that in Fig. 3b is obtained, and the pulse intensity is chosen to operate within the multistable regime. Arrows mark the pulse arrival times, and their orientation encodes the excitation phase. Depending on the excitation history, sixteen distinct oscillating states can be produced. From top left to bottom right, the panels correspond to the sixteen possible bit encodings from  $|0000\rangle$  to  $|1111\rangle$ . All remaining parameters are the same as in Fig. 3b. The colour scales have been saturated to one tenth of the maximum peak intensity across all panels.

Feynman-Kac theorem [21]. We are not aware of other works using it to model continuum systems in the litera-

ture, but a straightforward limiting procedure [31] results in the stochastic evolution equations

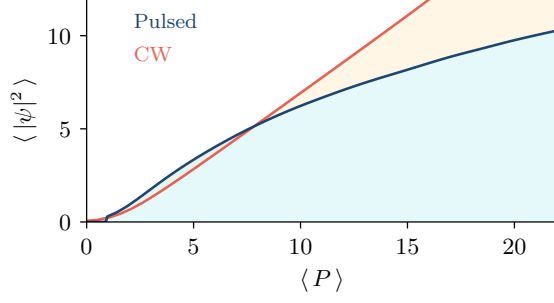


FIG. A2. **Optical Limiter Generalization.** b) A 1D tau-ochrone under non-resonant gain pulsed excitation. Parameters were the same as in Fig. 3a, with  $\alpha_{\text{NL}} = 0.3$ . We compare to the case of CW non-resonant gain in the same setup.  $\langle P \rangle$  represents the spatially integrated and time averaged gain.

$$\frac{d\psi_p(\mathbf{x})}{dt} = -\frac{i}{2}(\mathbf{x}^2 - \nabla^2 - 2\Delta - i\gamma + 2\alpha\psi_p^+(\mathbf{x})\psi_p(\mathbf{x}))\psi_p(\mathbf{x}) - iF(\mathbf{x}) + \sqrt{-i\alpha}\psi_p(\mathbf{x})\xi(\mathbf{x}, t) \quad (\text{A15})$$

$$\frac{d\psi_p^+(\mathbf{x})}{dt} = +\frac{i}{2}(\mathbf{x}^2 - \nabla^2 - 2\Delta + i\gamma + 2\alpha\psi_p^+(\mathbf{x})\psi_p(\mathbf{x}))\psi_p^+(\mathbf{x}) + iF(\mathbf{x}) + \sqrt{+i\alpha}\psi_p^+(\mathbf{x})\xi^+(\mathbf{x}, t) \quad (\text{A16})$$

where  $\xi, \xi^+$  are real-valued Wiener noise processes, satisfying

$$\xi(\mathbf{x}, t)\xi(\mathbf{x}', t') = \delta(t - t')\delta^2(\mathbf{x} - \mathbf{x}') \quad (\text{A17})$$

$$\xi^+(\mathbf{x}, t)\xi^+(\mathbf{x}', t') = \delta(t - t')\delta^2(\mathbf{x} - \mathbf{x}') \quad (\text{A18})$$

$$\xi(\mathbf{x}, t)\xi^+(\mathbf{x}', t') = 0 \quad (\text{A19})$$

We note that, since the noise coefficients in (A15) are non-constant, it is important to interpret them in the Ito sense for analytics or numerics [27, 28].

As in Fig 1, the setup is circularly symmetric. We will assume the same for the quantum solution, i.e.  $\psi_p(\mathbf{x}) = \psi_p(r)$ . This approximation amounts to neglecting scattering into the modes of finite angular momentum. Under the scheme considered however, such modes that break circular symmetry would have vanishing overlap with the region  $r \approx 0$  where the nonlinearity that could cause scattering becomes significant. Integrating out the angle  $\theta$ , the integration measure becomes  $\int d^2\mathbf{x} = \int 2\pi r dr$ .

In the following, we set  $\Delta = \omega_p - \omega_c = \omega$ , i.e. we drive on resonance with the ground state frequency of the 2D harmonic trap, to offset the trivial phase evolution of the linear system. In the classical limit, Eqs. (A15) collapse to a single deterministic Gross-Pitaevskij equation similar to (A6):  $\psi_p \leftrightarrow \psi$  while  $\psi_p^+ \leftrightarrow \psi^*$ .

For our simulations, we first initialize the system by an initial  $M_{\text{init, class}} = 1000$  of such pulses with this classical evolution, starting from the vacuum to converge to the steady-state solution of the mean field. This is in turn

taken as initial state for the quantum evolution.  $N_{\text{traj}} = 100$  independent phase space trajectories  $n$  are each evolved by (A15) for another  $M_{\text{init, quant}} = 100$  pulses, so that the quantum fluctuations reach the steady state as well. The trajectories are then each further evolved for another  $M = 100$  pulses  $m$  while the time-dependent results  $\psi_p^{(n)}(t), \psi_p^{+(n)}(t)$  are recorded. Treating this as time multiplexing of individual pulses of time  $\pi$  each, we can rearrange the results as  $\psi_p^{(n,m)}(\underline{t}), \psi_p^{+(n,m)}(\underline{t})$  where  $\underline{t} = t \bmod \pi$ . This leads to a total of  $M \times N_{\text{traj}}$  pulse evolutions to consider.

In the Positive P framework, normally ordered equal-time correlation functions are obtained as a statistical averages over trajectories:

$$\langle \hat{\psi}^\dagger(r)\hat{\psi}(r) \rangle = \text{Re}[\psi_p^+(r)\psi_p(r)]_{n,m} \quad (\text{A20})$$

$$\langle \hat{\psi}^\dagger(r)\hat{\psi}^\dagger(r')\hat{\psi}(r')\hat{\psi}(r) \rangle = \text{Re}[\psi_p^+(r)\psi_p^+(r')\psi_p(r')\psi_p(r)]_{n,m} \quad (\text{A21})$$

Using (A20) obtain the expectations displayed in Fig A3. In panel a) we observe that the spatial distribution of photons is in agreement with the mean-field predictions. In panel b, we plot

$$G_2(\mathbf{x}, t) = \frac{\int d^2\mathbf{x}' \langle \hat{\psi}^\dagger(\mathbf{x}, t)\hat{\psi}^\dagger(\mathbf{x}', t)\hat{\psi}(\mathbf{x}', t)\hat{\psi}(\mathbf{x}, t) \rangle}{\langle \hat{\psi}^\dagger(\mathbf{x}, t)\hat{\psi}(\mathbf{x}, t) \rangle \int d^2\mathbf{x}' \langle \hat{\psi}^\dagger(\mathbf{x}', t)\hat{\psi}(\mathbf{x}', t) \rangle}, \quad (\text{A22})$$

which indicates the relative probability of finding a second photon at point  $\mathbf{x}$  given the presence of another photon somewhere in the trap.

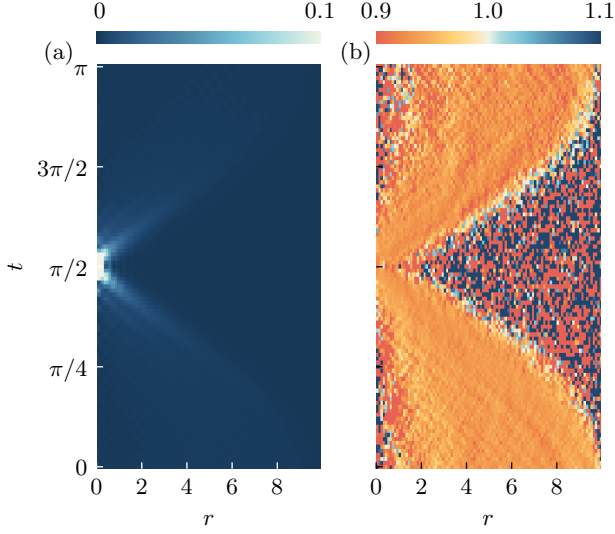


FIG. A3. **Pulse evolution in the quantum model.** (a): Intensity  $\langle \hat{\psi}^\dagger(x,t)\hat{\psi}(x,t) \rangle$  at  $y=0$ , confirming the picture that was obtained with mean-field theory 2. Relative probability (b)  $G_2(x,t)$  of finding additional photons at point  $x$  given the finite intensity anywhere in the trap ((A22)), displaying antibunching wherever there is significant intensity. Noise nominates at  $r,t$  values with vanishingly small intensity. Parameters  $\alpha = 0.1$ ,  $F_0 = 0.5$

Similarly one obtains the second-order correlation function of the full trap  $g^{(2)}(t)$  Eq. (4). In fact, since number statistics are unaffected in between pulses (there is only a uniform, linear decay at rate  $\gamma$ ), a final average of  $g^{(2)}$  over  $\underline{t}$  is taken for the results presented in Fig. 5.

*FDTD simulations.* —

As an example design for implementation of a photonic tautochrone, we choose a planar  $\lambda/2$  microcavity (where  $\lambda$  is an optical wavelength) with a quantum well in the strong coupling regime. The polaritonic modes of the system experience a parabolic potential, created using a reservoir of excitons[7, 15]. By spatially modulating a non-resonant laser, the spatial distribution of excitons can be controlled to design a quadratically increasing exciton density. The effective polariton potential is induced by the repulsive Coulomb interaction between the polaritons and the reservoir excitons.

In order to simulate from first principles the dynamics of this tautochrone system in both the linear and non-linear regimes, we use our self-developed Non-Linear Bloch-Maxwell FDTD algorithm [16, 17]. We chose to simulate the behaviour of the 1D tautochrone using a 2D FDTD grid as the computational resources and time required for 3D would be too demanding due to the relatively large size of the system. The reservoir density

is assumed fixed. The exciton dipole moment is chosen to be only in plane and the polarization of light is chosen to be transverse electric, i.e.,  $(H_x, E_y, H_z)$ ;  $y$  is taken as a translationally symmetry direction;  $z$  is the growth direction;  $x$  is the direction in which the potential changes. The Maxwell-Bloch equations considered can be expressed as:

$$\nabla \times \mathbf{H} = \epsilon \frac{\partial \mathbf{E}}{\partial t} + \mathbf{J}_b \quad (\text{A23})$$

$$\nabla \times \mathbf{E} = -\mu_0 \frac{\partial \mathbf{H}}{\partial t}, \quad \mathbf{J}_b = \frac{\partial \mathbf{P}}{\partial t} \quad (\text{A24})$$

$$i\hbar \frac{\partial P_y}{\partial t} = E_\chi P_y - gE_y + \alpha(N + N_D)P_y \quad (\text{A25})$$

$$\frac{\partial N}{\partial t} = -2 \text{Im}(\Omega E_y P_y^*) \quad (\text{A26})$$

$$\frac{\partial N_D}{\partial t} = 0 \quad (\text{A27})$$

where  $\mathbf{E}$  and  $\mathbf{H}$  are respectively the electric and magnetic fields,  $J_b$  is the bound electric current density,  $\epsilon$  is the spatial distribution of the permittivity,  $\mu_0$  is the vacuum permeability,  $E_\chi$  is the exciton resonance energy,  $g$  is the effective light matter coupling coefficient,  $\alpha$  is the exciton-exciton interaction constant,  $N$  is the spatial distribution of the exciton density and  $N_D$  is the spatial distribution of excitons in the reservoir analog to the potential.

The considered microcavity is a 134.2 nm thick  $\text{Ga}_{0.05}\text{Al}_{0.95}\text{As}$  layer with refractive index  $n = 3.05$ . The mirrors are designed with distributed Bragg reflectors composed of 20 pairs of  $\text{Ga}_{0.05}\text{Al}_{0.95}\text{As}$  and  $\text{Ga}_{0.8}\text{Al}_{0.2}\text{As}$ , with respective thicknesses of 67.1 nm and 57.6 nm. The refractive index of  $\text{Ga}_{0.8}\text{Al}_{0.2}\text{As}$  is  $n = 3.55$ . A 20 nm thick GaAs layer with refractive index  $n = 3.62$  forms a quantum well in the center of the microcavity. The total length of the cavity is  $L = 50 \mu\text{m}$ .

We first calculate the dispersion of the system with  $N_D = 0$ .  $g$  is set such that the Rabi splitting (energy difference between the lower and upper polariton modes at zero detuning) is 18 meV. The exciton energy is set at  $E_\chi = 1.50$  eV, the fundamental cavity mode energy is  $E_c = 1.497$  eV giving an effective detuning of 3 meV. The dispersion is calculated following the same procedure as in [16, 17].

In order to simulate the dynamics of a pulse, the optical pump is modeled in the FDTD framework as an incident electromagnetic wave injected from the top boundary and propagating normal to the GaAs microcavity plane. The pump is injected as an electric field at the edge of the regular grid:

$$E_y^{\text{pump}} \propto \exp\left(-\frac{(t-t_0)^2}{\tau^2}\right) \exp\left(-\frac{iE_0}{\hbar}(t-t_0)\right) \exp\left(-\frac{x^2}{W^2}\right) \quad (\text{A28})$$

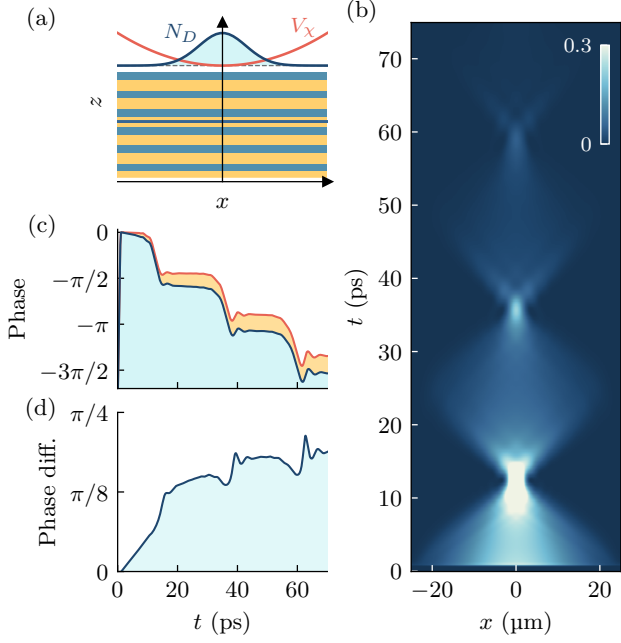


FIG. A4. **FDTD simulation of a tautochrone.** (a) A quantum well is embedded between two Bragg mirrors, forming a planar microcavity. The system is initialised with a Gaussian reservoir population  $N_D$ , and the excitonic component is subject to a quadratic potential  $V_x$ . (b) Time evolution of the electric-field intensity  $|E(x,t)|^2$ , showing that the focusing signal is lost after approximately 70 ps due to the finite photon dwelling time in the microcavity. The colour scale is saturated to 0.3 of the maximum intensity. (c) Phase of the electric field  $E(x=0,t)$  defined in the rotating frame associated with the ground state of the excitonic potential, shown with (red) and without (blue) nonlinear interactions. (d) Phase difference between the linear and nonlinear evolutions in the presence of a quadratic potential, showing progressively smaller phase jumps at successive focusing events due to the reduced nonlinear interaction as the intensity decays.

where  $\tau = 200$  fs is the pulse duration,  $W = 20$   $\mu\text{m}$  is the spot size,  $t_0 = 5\tau$  is the pulse arrival time and  $E_0 = 1.487$  eV is the pulse central energy. In the linear regime, the amplitude of the pump is chosen arbitrarily small such that no blueshift can be observed with or without the tautochrone potential. In the non-linear regime the amplitude is chosen such that the associated blueshift without the tautochrone potential (i.e. for a depleted reservoir) is smaller than the linewidth. The reservoir is set such that it induced a parabolic blueshift of the exciton:

$$N_D(x) = \frac{V_x^{\max}}{\alpha} \frac{4x^2}{L^2} \quad (\text{A29})$$

In order to stay consistent with experimental reports in GaAlAs cavities we set the maximum exciton blueshift to 10 meV [7, 23]. We then reproduce the tautochrone ef-

fect, calculated using Eq. (1). Unlike in the main text, we do not reamplify the signal after half a period. Consequently, the intensity of the signal decreases with time and the phase gain at each focus decreases with time accordingly.

These simulations confirm from first principles on the photonic side that results obtained within the Gross-Pitaevskij framework can be faithfully realized in a photonic structure.